Conjugated Polyelectrolyte Doped Perovskite Films with Enhanced Photovoltaic Performance and Stability

Helin Wang[a,b,#], Jiatao Wu[b,c,#], Jun Song[a,*], Junle Qu[a], Jiarong Lian[a], Peng-Cheng Qian[d,*],

Wai-Yeung Wong[b,e,*]

[a]Center for Biomedical Optics and Photonics (CBOP) & College of Physics and Optoelectronic Engineering, Key Laboratory of Optoelectronic Devices and Systems, Shenzhen University, Shenzhen 518060, Guangdong, P. R. China.

[b]Department of Applied Biology and Chemical Technology, The Hong Kong Polytechnic University (PolyU), Hung Hom, Hong Kong, P. R. China.

[c]College of Chemistry and Chemical Engineering, Shenzhen University, Shenzhen 518060, Guangdong, P. R. China.

[d]Key Laboratory of Environmental Functional Materials Technology and Application of Wenzhou City, Institute of New Materials & Industry Technology, College of Chemistry & Materials Engineering, Wenzhou University, Wenzhou 325035, Zhejiang, P. R. China.

[e]PolyU Shenzhen Research Institute, Shenzhen 518057, Guangdong, P. R. China.

[*] Corresponding authors.

[#] H. Wang and J. Wu contributed equally to this work.

E-mail: songjun@szu.edu.cn (J. Song), wai-yeung.wong@polyu.edu.hk (W.-Y. Wong), qpc@wzu.edu.cn (P.-C. Qian).

Keywords: conjugated polyelectrolyte; dopant; surface passivation; electron transport; perovskite solar cell.

Abstract: Perovskite solar cells (PSCs) have achieved great success in the past few years because of outstanding photovoltaic performance. However, the existence of electronic trap states in the perovskite film is an obstacle for the fabrication of high-performance and stable PSCs. Herein, a linear conjugated polyelectrolyte was developed and employed as a dopant to improve the performance and stability of the perovskite film. The PPNNA doping can passivate surface defects to reduce the electronic trap states in the perovskite film, while simultaneously enhancing the electron extraction and transport to achieve high-efficiency solar cells. Furthermore, the PPNNA-doped perovskite film shows better stability from efficient surface passivation. The optimal 0.4% PPNNA-doped device exhibits better photovoltaic efficiency (20.38%) with enhanced device stability as compared to the control device (18.51%). This novel method by doping with the conjugated polyelectrolyte provides a pathway to fabricate high-efficiency and stable inverted PSCs.

1. Introduction

Perovskite materials have attracted attention from researchers in materials science owing to their excellent photovoltaic properties [1-3]. The recent photovoltaic efficiency of solar cells by using high-performance perovskite materials has climbed from 3.8% to 25.2% [4-6], which suggests perovskite solar cells (PSCs) as a viable clean energy technology. However, poor device stability has slowed the commercialization of the PSCs [7-9]. The film morphology and electronic properties are the critical issues that impact the performance and stability of PSCs [10-16]. The existence of electronic trap states is caused by pinholes or ionic defects in the perovskite film [17]. These traps are located at the surface of the perovskite film or near grain boundaries, and promote non-radiative recombination losses and severely reduce the exciton lifetime and the photoluminescence (PL) yield [18]. Moreover, these traps also facilitate accelerated degradation of the perovskite film by moisture or oxygen permeation [19]. Several efforts have tried to reduce the electronic trap states, such as increasing the

perovskite grain size [20], reducing the grain boundary [21], and using interface engineering between layers [22-24]. These strategies tune the morphology of the perovskite film and enhance the interface contact, thereby inhibiting charge recombination and extending the exciton lifetime. Nevertheless, ionic migration is prone to occur in the perovskite film under the influence of external thermal or illuminated activation resulting in the non-stoichiometric decomposition inside the perovskite crystal. Halide vacancies and under-coordinated lead ions are also the main sources of the electronic trap states [25]. Therefore, efficient passivation of electronic trap states marks a key challenge to elevate the performance and stability of PSCs.

Small organic molecules or polymers can be used to suppress electronic trap states by doping or interface engineering methods [26-29]. Compared with organic small molecules, polymers with interesting optoelectronic properties and excellent film morphology provide a new pathway to improve the photovoltaic performance and stability of the perovskite films [30, 31]. These polymers can establish a two-dimensional network structure in the film and aid in the formation of pinhole-free and compact perovskite films [32]. Besides, heteroatoms (such as N, O, S, etc.) and active groups (such as hydroxyl, amino, carboxyl, etc.) in the molecular structure allow intermolecular interactions with under-coordinated lead ions to suppress ion migration and surface defects for better performance [33, 34]. But there are rare research studies on the conjugated polyelectrolyte doped perovskite film. In comparison with the commercially available polymer dopants (such as PMMA, etc.) [35], conjugated polyelectrolytes have a longer conjugated backbone, which facilitates better charge extraction and transport. Furthermore, conjugated polyelectrolytes are used as the hole transport layer or the interfacial layer or the dopant in the PSCs, which could efficiently reduce charge recombination and improve the interface contact [36-41]. Accordingly, we are eager to develop the conjugated polyelectrolyte containing heteroatoms or active groups, which facilitates efficient perovskite surface passivation to improve the device performance in PSCs.

In this work, we designed and synthesized a novel conjugated polyelectrolyte, namely poly(meta-phenyleneethynylene)s (PPNNA) as a dopant to tune the device performance and stability. PPNNA is comprised of two repeat units 1,4-(6-(triethylammonio)-hexyl)oxy)-para-diethynylbenzene and 2,6-nitroaniline. As a dopant, PPNNA has the following advantages. (a) The longer linear conjugated skeleton promotes the directional movement of the charges. (b) Long side chains increase the solubility of PPNNA. (c) Quaternary ammonium salts in the side chains further heighten the carrier mobility of PPNNA. (d) The amino and ammonium groups in the molecular skeleton could reduce undercoordinated lead ions or halides and minimize surface defects in the perovskite film, which helps to prevent the charge recombination and energy losses in PSCs [42, 43]. Furthermore, compared with the previous works by the organic small molecular additives [44-47], the PPNNA doping not only could reduce the electronic trap states but also facilitate efficient charge extraction and transport, which contributes to the balance carrier transport to improve the fill factor (FF) in PSCs. Therefore, PPNNA was applied as a dopant to fabricate inverted PSCs. Our results showed the 0.4% PPNNA-doped device exhibited a power conversion efficiency (PCE) of 20.38% together with better device stability, which suggests that PPNNA as a dopant could improve the perovskite film, and it has a good application prospect in the PSC field.

2. Results and Discussion

The synthetic route and methodology of PPNNA are shown in **Scheme 1** (see Supporting Information). Briefly, 1,4-bis((6-bromohexyl)oxy)-2,5-diiodobenzene (monomer 1) was synthesized *via* the bromination reaction. Subsequently, 1,4-bis((6-bromohexyl)oxy)-2,5-diethynylbenzene (monomer 2) was obtained *via* the Sonogashira coupling reaction with a moderate yield. Afterward, the key intermediate 7-(2,5-diethynyl-4-((6-(triethylammonio)-hexyl)oxy)phenoxy)-N,N,N-triethylheptan-1-aminium (monomer 3) was obtained *via* quaternization reaction with a 92% yield. Finally, the conjugated polyelectrolyte PPNNA was

prepared *via* the Sonogashira coupling reaction of 2,6-diiodo-4-nitroaniline and monomer 3. The chemical structures of intermediates and PPNNA were characterized by ^{1}H NMR as shown in **Figure S1**. The number average molecular weight (M_n), weight average molecular weight (M_w), and polydispersity index (PDI) were determined by gel permeation chromatography (GPC) to be 7930 Da, 10900 Da, and 1.37 for PPNNA, which indicates that the polymerization of PPNNA was successful. The conjugated polyelectrolyte PPNNA was soluble in the highly polar organic solvents, such as DMF and DMSO, because of amino groups and quaternary ammonium salts in the molecular structure.
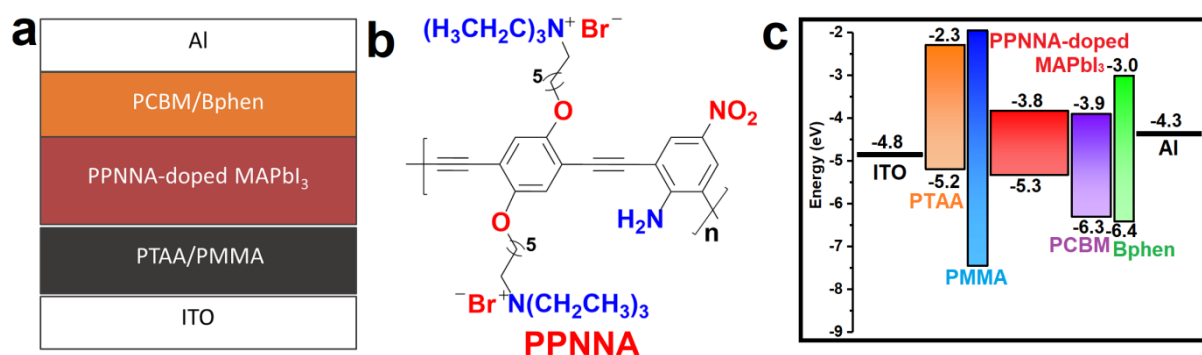

Figure 1. (a) The device configuration of inverted PSCs for this work; (b) molecular structure of monomer structure for the conjugated polyelectrolyte PPNNA; (c) energy level diagrams of materials.

Figure S2 shows the UV-vis and PL spectra of PPNNA. There are two absorption bands at 280-330 nm and 400-450 nm in the DMSO solution. The absorption band at 280-330 nm was ascribed to the aromatic π-π* transition, and the stronger band at 400-450 nm was attributed to the intramolecular charge transfer (ICT) between the hydroquinone donor and 4-nitroaniline acceptor. The absorption maximum located at 441 nm and the maximum emission located at 461 nm, which implies that the ICT effect results in a small Stokes shift. The thermal properties of PPNNA were explored by differential scanning calorimeter (DSC)

(**Figure S3**). An exothermic peak of PPNNA was found at 51.3 °C. This low exothermic temperature partly originates from a strong crystallinity of the linear conjugated framework. Thermogravimetric analysis (TGA) was measured to investigate the thermal stability of PPNNA as shown in **Figure S4**. The 6% weight-loss temperature of PPNNA was located at 220 °C under a nitrogen atmosphere, which suggests that PPNNA has moderate thermal stability. The current density-voltage (*J-V*) traces of electron-only devices were measured to estimate the electron mobility of PPNNA. The space charge limited current (SCLC) device architecture is ITO/ZnO/PPNNA/Ca/Al. The electron mobility of PPNNA was calculated to be 2.42×10^{-4} cm^2 V^{-1} s^{-1} as shown in **Figure S5**, implying that PPNNA exhibits appropriate electron mobility and facilitates efficient charge transport in PSCs.

The inverted PSCs were fabricated with the device architecture of ITO/PTAA:F4-TCNQ/PMMA/MAPbI$_3$/PCBM/Bphen/Al as shown in **Figure 1a**. PTAA and PCBM were employed as hole and electron transport layers, respectively. F4-TCNQ was a p-type dopant and enhanced the conductivity of the PTAA film mainly owing to the strong electron-withdrawing ability of F4-TCNQ. Besides, polymethyl methacrylate (PMMA) and 4,7-diphenyl-1,10-phenanthroline (Bphen) were used as a passivation layer and a thin buffer layer, respectively. The control device without PPNNA doping was also fabricated. The energy level diagrams of the various materials are depicted in **Figure 1c**. The energy levels of MAPbI$_3$ and 0.4% PPNNA-doped MAPbI$_3$ films were determined by the ultraviolet photoelectron spectrometer (UPS) method, and the results are summarized in **Table S1**. The UPS spectra of the two films are depicted in **Figure S6**. As a consequence, the CB and VB of MAPbI$_3$ were slightly increased after PPNNA doping, suggesting that the appropriate energy level of the 0.4% PPNNA-doped MAPbI$_3$ film is more helpful for efficient charge extraction and transport.

The *J-V* curves were used to measure the doping concentration effect on device performance as shown in **Figure 2a**, and the corresponding results were summarized in **Table**

S2. As the doping concentration raised from 0 to 0.4%, the device efficiency was improved. The PCE value for the optimal device based on 0.4% PPNNA doping was 20.2%, which was superior to that of the control device (18.2%). This enhancement is clear from the increased open-circuit voltage (V_{oc}) and FF, both of which could be attributed to efficient surface passivation and reduced charge recombination (see **Figures 4b** and **4e**). When the doping amount of PPNNA was increased to 0.8%, the device efficiency decreased, which was caused by poor film morphologies. These results suggest that there is an optimal doping amount of PPNNA that can enhance the MAPbI$_3$ film and obtain superior device performance.
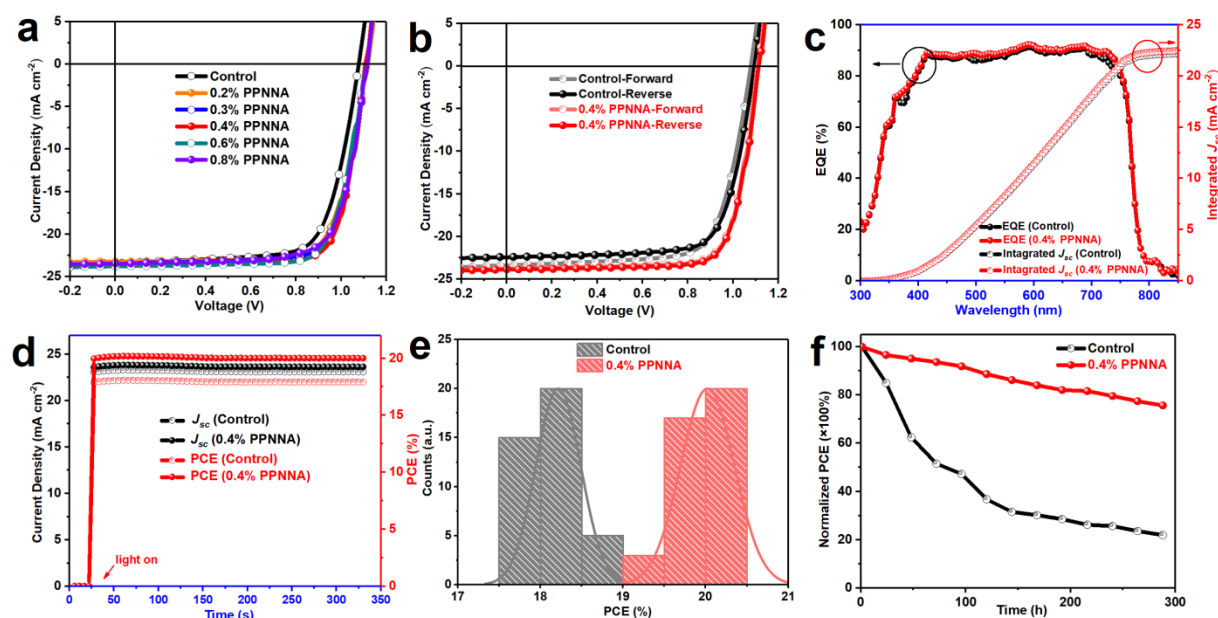

Figure 2. (a) *J-V* characteristics of the PSCs doped with different PPNNA concentrations; (b) *J-V* characteristics under different scanning directions; (c) corresponding EQEs and the integrated products of EQE curves; (d) the stabilized J_{sc} and PCE traces; (e) the statistics of the PCE distribution; (f) normalized PCEs of the encapsulated control and doped devices after aging stored in dark under 25% humidity condition.

Figure 2b presents the champion *J-V* characteristics for the control and 0.4% PPNNA-doped devices, and the optimal device parameters are summarized in **Tables 1** and **S3**. The

optimal control device showed a short-circuit current density (J_{sc}) of 23.31 mA cm^{-2}, a V_{oc} of 1.099 V, and a FF of 72.22%, yielding a PCE of 18.51%. After 0.4% PPNNA doping, the PCE improved to 20.38% along with increases of all the key J-V parameters (J_{sc} = 23.86 mA cm^{-2}, V_{oc} = 1.120 V, FF = 76.29%). The enhanced electron extraction, transport, and interface contacts contribute to the increased J_{sc} and FF, which stems from the high electron mobility of PPNNA and efficient surface passivation (see **Figures 3** and **4**). The V_{oc} increased about 20 mV from 1.099 V to 1.120 V, and this increased voltage difference is attributed to fewer electronic trap states and suppressed non-radiative recombination losses (see **Figure 4f**). The PPNNA doping effects on the hysteresis in PSCs were investigated with J-V curves as shown in **Figure 2b**. The doped device exhibited a smaller hysteresis than that of the control device. From literature reports [48, 49], the hysteresis index (HI) value was found to be 0.0074 for the PPNNA-doped device while the HI value of the control device was 0.015, revealing that PPNNA doping provided negligible hysteresis for the inverted PSCs. This low HI for the doped device is closely related to efficient surface passivation (see **Figures 4b** and **4e**).

Table 1. Optimal device parameters of the PSCs without and with PPNNA doping.

Active layer	Scan direction	J_{sc} [mA cm^{-2}]	V_{oc} [V]	FF [%]	PCE [%]
Control	Forward scan	23.41	1.078	72.02	18.17
Control	Reverse scan	23.31	1.099	72.22	18.51
0.4% PPNNA	Forward scan	23.79	1.115	76.00	20.15
0.4% PPNNA	Reverse scan	23.86	1.120	76.29	20.38

The corresponding external quantum efficiency (EQE) values for the two devices were measured and displayed in **Figure 2c**. The integrated photocurrent densities from the EQE curves were in good agreement with the J-V results. The integrated photocurrent density increased to 22.49 mA cm^{-2} for the PPNNA-doped device compared with that of the control device (22.17 mA cm^{-2}) because of more efficient electron extraction and transport (see **Figures 4c** and **4f**). **Figure 2d** shows the steady-state J_{sc} and PCE traces at the maximum

power for the two best-performing devices. The stabilized J_{sc} and PCE were 23.62 mA cm^{-2} and 20.02% for the PPNAA-doped device in comparison with 23.09 mA cm^{-2} and 17.92% for the control device. Higher stabilized J_{sc} and PCE values indicate that PPNNA doping could enhance the MAPbI$_3$ film, thus improving the photovoltaic performance.

To investigate the reproducibility of the two PSCs, 40 separate devices in the same batch were fabricated, and the statistical analysis data are shown in **Figure 2e**. The standard deviations were relatively small pointing to the excellent reproducibility of the two PSCs. A higher PCE average value for the PPNNA-doped devices was found to be 20.02±0.33%, compared with that of the control device (18.21±0.27%). Device stability was tested placing two of the best-performing devices in the dark with a relative humidity of 25%. The J-V curves were measured at intervals of 24 h under standard conditions (AM 1.5G sunlight, 100 mW cm^{-2}). **Figure 2f** shows that the PPNNA-doped device had exhibited long-term stability with an efficiency dropped to 75% of its initial value, as compared with a decline to 20% of the initial value for the control device after storage for 300 h. The decreased PCE values arise from instability and slow deterioration of the MAPbI$_3$ films, which indicates that PPNNA doping could protect or passivate the perovskite film to maintain device stability. The aluminum electrode has high reactivity and can accelerate ionic migration in the perovskite film, thereby promoting device instability. However, PPNNA doping reduces the electronic traps and prevents moisture or oxygen permeation into the perovskite film (**Figure 4f**). Hence, the PPNNA-doped perovskite film exhibited better stability than the control film.

The PPNNA-doped MAPbI$_3$ films were observed using atomic force microscopy (AFM) and scanning electron microscopy (SEM) to evaluate the surface morphologies of the perovskite film. Four AFM height images of the MAPbI$_3$ films with different doping concentrations are presented in **Figures 3a-3d**. The root-mean-square (RMS) roughness values were estimated to be 16.6, 13.7, 13.6, and 11.7 nm for the 0.0%, 0.2%, 0.4%, and 0.8% PPNNA-doped films, respectively. These RMS values indicate that with increased doping

concentrations, the perovskite films were smoother and more compact and that improved interface contact in PSCs. As the doping concentration increased, more PPNNA crystals could emerge near the surface of the perovskite films or grain boundaries. Therefore, the PPNNA doping provided efficient surface passivation and better charge transport. The AFM 3D images of the four films are depicted in **Figure S7**. The sizes of the grain boundaries decrease with increased doping concentrations. These results evince PPNNA as a good dopant for the formation of continuous and uniform MAPbI$_3$ films.
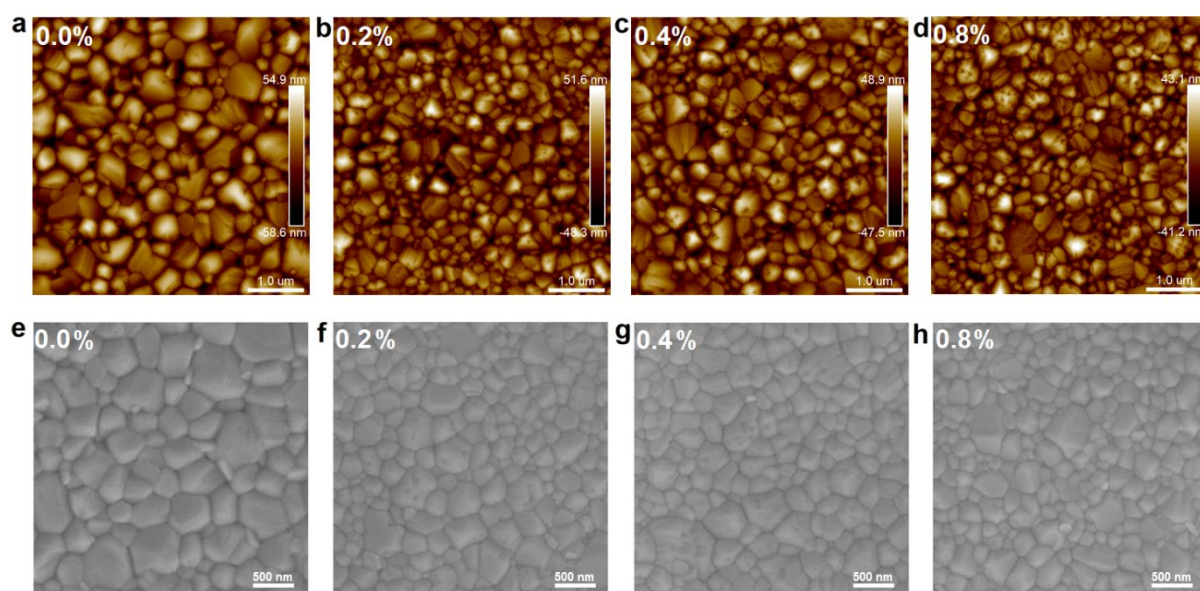

Figure 3. AFM height images of the 0.0% (a), 0.2% (b), 0.4% (c), and 0.8% (d) PPNNA-doped MAPbI$_3$ films; SEM top-view images of the 0.0% (e), 0.2% (f), 0.4% (g), and 0.8% (h) PPNNA-doped MAPbI$_3$ films.

Furthermore, the SEM top-view images of the four films are shown in **Figures 3e-3h**. The average grain sizes are 258, 247, 234, 216 nm for the 0.0%, 0.2%, 0.4%, and 0.8% PPNNA-doped perovskite films, respectively. The pure film exhibits larger crystal sizes than the doped films. But the pinholes on the surface of the doped films were slightly reduced compared with those on the pure film, which could be attributed to the formation of the more

10

homogeneous and compact films after PPNNA doping. The PPNNA crystals could be observed near the surface of the perovskite films in the SEM images (**Figures 3f-3h**), and these crystals were marked with red circles in **Figure S8**. Moreover, the SEM-based energy dispersive spectroscopy (EDS) was measured to explain the PPNNA distribution, and the corresponding SEM-EDS top-view images were shown in **Figure S9**. The bromine atoms in the molecular skeleton of PPNNA can be observed near the surface of the perovskite film, suggesting that it is evidence to further account for the PPNNA distribution in the doped perovskite film, which is in good agreement with the SEM and AFM results. The pinhole-free and compact film morphologies of the doped films were helpful for enhancing the device stability because of the suppression of moisture or oxygen permeation into the film. At the same time, the doped films after surface modification contributed to high device performance, which was closely associated with the *J-V* results. The above results illustrate that PPNNA could be used as a perovskite dopant to improve the film morphologies and interface contact, thus achieving the high-efficiency and stable inverted PSCs.

The crystallization of the $MAPbI_3$ films with or without doping was compared by X-ray diffraction (XRD) and shown in **Figure 4a**. Strong diffraction peaks located at 14.1°, 20.0°, 23.5°, 24.5°, 28.4°, 31.9°, 40.7°, and 43.1°for 2θ scan were observed, corresponding to the planes of (110), (112), (211), (202), (220), (222), (224), and (314) of the $MAPbI_3$ perovskite, which was in good agreement with the previous reports [20]. According to the full width at half maximum of XRD main peaks, the grain sizes were estimated to be 238, 226, 217, and 214 nm for the 0.0%, 0.2%, 0.4%, and 0.8% PPNNA-doped $MAPbI_3$ films, respectively, which is in accordance with SEM results. The diffraction peaks of three doped films are similar to those of the pure $MAPbI_3$ film however the peak intensity for three doped films is decreased. These results suggest that smaller and more compact $MAPbI_3$ crystallite sizes were obtained, which agrees with the AFM and SEM findings. X-ray Photoelectron Spectroscopy (XPS) core-level spectra were collected for the pure and 0.4% doped films. As shown in

Figure 4b, the Pb $4f_{7/2}$ and Pb $4f_{5/2}$ peaks were located at 143.6 eV and 138.7 eV for the pure film. But the peak positions were shifted by 0.2 eV toward the low binding energy side after PPNNA doping. The I 3d core-level peak position shifts were similar to those of Pb 4f as presented in **Figure S10**. Both of these shifts are attributed to the intermolecular interaction between PPNNA and $MAPbI_3$. Therefore, this is direct evidence of the existence of efficient surface passivation.

The stable PL spectra were measured for the pure $MAPbI_3$ film, the 0.4% doped film, and those coated by PCBM (**Figure 4c**). The PL intensity of the doped film was lower compared with the pure film, indicating that PPNNA doping strengthens the charge extraction. To further discern the origins of PL differences, two PCBM-coated films with and without doping were measured. With PPNNA doping, the PCBM-coated film exhibited significant PL quenching, which demonstrates that PPNNA doping is a positive influence for efficient electron extraction in PSCs. The time-resolved photoluminescence (TRPL) was carried out for the $MAPbI_3$/PCBM and PPNNA-doped $MAPbI_3$/PCBM films as shown in **Figure S11**, and the TRPL decays were modelled using a biexponential decay function. Compared with the $MAPbI_3$/PCBM film, the PL decay time of the doped film significantly decreases. The shortened t_1 and t_2 demonstrates that the PPNNA doping facilitates efficient electron extraction and suppresses non-recombination losses in PSCs. These TRPL results are in good agreement with the higher V_{oc} in the doped device.

To gain a deeper insight into the enhancement of the device performance after PPNNA doping treatment, the corresponding photophysical processes in PSCs were evaluated by measuring the change of the J_{sc} or V_{oc} *versus* light intensity (*P*) traces. As depicted in **Figure 4d**, there are two traces with the dependence of *P* on the J_{sc} and their linear fitting models. According to the J_{sc} *versus* P^{α}, the scaling factors (α) were found to be 0.94 and 0.97 for the control and doped devices, respectively, implying that PPNNA doping could reduce the bimolecular recombination, which was attributed to efficient passivation and interface

12

contacts. The improvement of device efficiency was further evidenced by the V_{oc} response under different light intensities as shown in **Figure 4e**. The ideality factor originated from the slope of the V_{oc} *versus* P traces [50], which is closely associated with trap-assisted recombination in PSCs. Hence, the control device exhibited a factor of 1.41 kT q^{-1}, whereas that of the doped device decreased to 1.31 kT q^{-1}. These results further demonstrate that PPNNA doping suppresses energy losses in PSCs caused by the trap-assisted recombination.
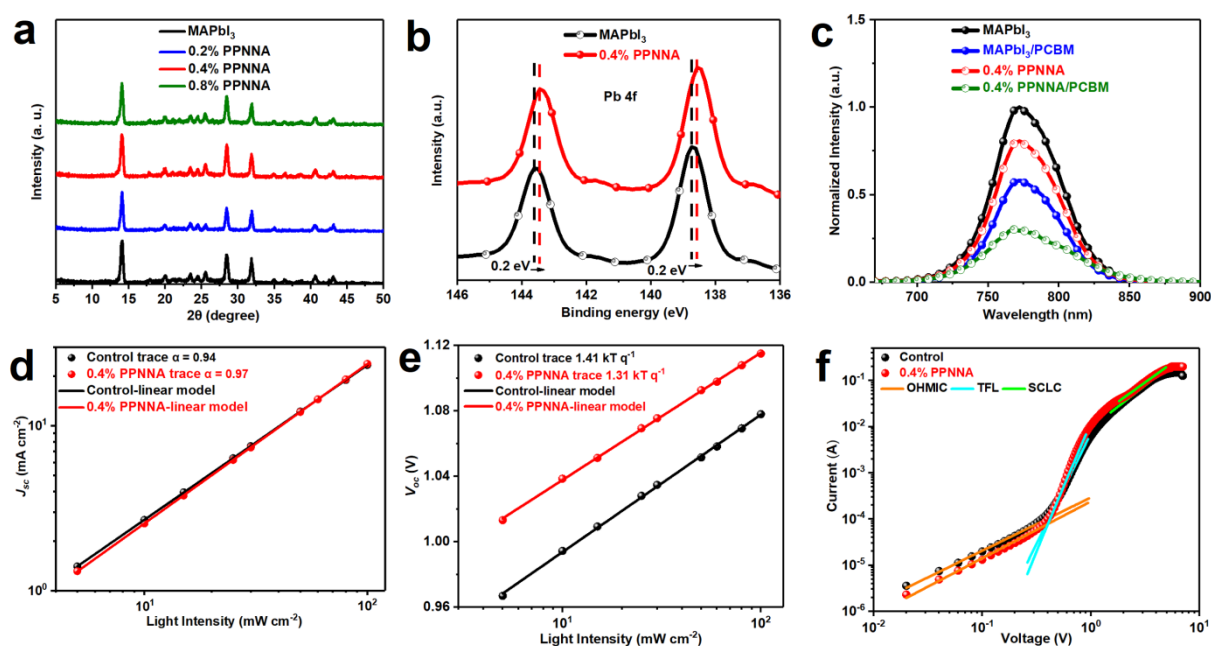
Figure 4. (a) XRD patterns of MAPbI$_3$ films doped with different PPNNA concentrations; (b) XPS spectra of Pb (4f) for pure MAPbI$_3$ and 0.4% PPNNA-doped films; (c) steady-state PL spectra for pure MAPbI$_3$ film, 0.4% PPNNA-doped film, and those coated by PCBM; (d) corresponding J_{sc} *versus* light intensity traces (symbols) together with the linear fitting model (solid lines); (e) corresponding V_{oc} *versus* light intensity (symbols) together with the linear fitting model (solid lines); (f) corresponding *J-V* traces of the electron-only perovskite-based SCLC devices with different active layers.

At last, the trap density (N_{trap}) and electron mobility (μ_e) for the two devices were estimated by using the SCLC method. The electron-only SCLC devices including the structural backbone of ITO/SnO$_2$/MAPbI$_3$/PCBM/Bphen/Al were fabricated. **Figure 4f** shows two *J-V* traces and their linear fitting models. The *J-V* traces have three distinct regions of behavior for calculating the corresponding trap density and electron mobility in the device, and the results are summarized in **Table 2** [51-53]. The trap densities of 1.65×10^{15} and 1.80×10^{15} cm^{-3} for the control and PPNNA-doped devices together with corresponding trap-filled limit voltages (V_{TFL}) of 0.38 and 0.42 V, respectively. The above results confirm that efficient surface passivation and excellent film morphology contribute to the drop of trap-assisted recombination, which is in good agreement with the XPS and photophysical results. The electron mobilities were estimated to be 0.029 cm^2 V^{-1} s^{-1} for the PPNNA-doped device in comparison with the control device (0.020 cm^2 V^{-1} s^{-1}). This improved mobility allows more efficient electron transport could aid the enhanced *J*$_{sc}$ and PCE in PSCs. These data and analysis support that PPNNA doping is a viable methodology for significantly improving the perovskite film for better photovoltaic performance.

Table 2. Trap density and electron mobility of control and 0.4% PPNNA-doped devices.

Active layer	V_{TFL} [V]	N_{trap} [cm^{-3}]	μ_e [cm^2 V^{-1} s^{-1}]
Control	0.42	1.80×10^{15}	0.020
0.4% PPNNA	0.38	1.65×10^{15}	0.029

3. Conclusion

In summary, a novel conjugated polyelectrolyte (PPNNA) was synthesized and used as a dopant to reduce the electronic trap states in the perovskite film. The SEM and AFM investigations reveal that the PPNNA crystals are mainly distributed near the surface of the perovskite film and grain boundaries. Furthermore, PPNNA doping can improve the

formation of the perovskite film and afford suitable surface modification. The photophysical and SCLC results suggest that PPNNA doping can suppress charge recombination and decrease the trap density, both of which are helpful for diminishing energy losses and enhancing electron transport in PSCs. The best-performing PCE of 20.38% for the 0.4% PPNNA-doped device was compared with the control device (18.51%). Efficient surface passivation and interface contacts both contributed to better device stability for the 0.4% doped device. These findings in this work pave the path for conjugated polyelectrolytes to serve as an efficient dopant to achieve better stability and higher performance PSCs.

Supporting Information

Supporting Information is available from the ELSEVIER.

Acknowledgements

Conflict of Interest

The authors declare no conflict of interest.

References

[1] W. S. Yang, B.-W. Park, E. H. Jung, N. J. Jeon, Y. C. Kim, D. U. Lee, S. S. Shin, J. Seo, E. K. Kim, J. H. Noh, S. Seok, Iodide management in formamidinium-lead-halide-based perovskite layers for efficient solar cells, Science 356 (2017) 1376-1379.

[2] W. S. Yang, J. H. Noh, N. J. Jeon, Y. C. Kim, S. Ryu, J. Seo, S. Seok, High-performance photovoltaic perovskite layers fabricated through intramolecular exchange, Science 348 (2015) 1234-1237.

[3] Q. Fu, X. Tang, B. Huang, T. Hu, L. Tan, L. Chen, Y. Chen, Recent progress on the long-term stability of perovskite solar cells, Adv. Sci. 5 (2018) 1700387.

[4] M. Liu, M. B. Johnston, H. J. Snaith, Efficient planar heterojunction perovskite solar cells by vapour deposition, Nature 501 (2013) 395-398.

[5] H. Zhou, Q. Chen, G. Li, S. Luo, T.-b. Song, H.-S. Duan, Z. Hong, J. You, Y. Liu, Y. Yang, Interface engineering of highly efficient perovskite solar cells, Science 345 (2014) 542-546.

[6] H. Min, M. Kim, S. Lee, H. Kim, G. Kim, K. Choi, J. H. Lee, S. Seok, Efficient, stable solar cells by using inherent bandgap of α-phase formamidinium lead iodide, Science 366 (2019) 749-753.

[7] S. S. Shin, S. J. Lee, S. I. Seok, Metal oxide charge transport layers for efficient and stable perovskite solar cells, Adv. Funct. Mater. 29 (2019) 1900455.

[8] T. Zhou, H. Lai, T. Liu, D. Lu, X. Wan, X. Zhang, Y. Liu, Y. Chen, Highly efficient and stable solar cells based on crystalline oriented 2D/3D hybrid perovskite, Adv. Mater. 31 (2019) 1901242.

[9] A. Rajagopal, K. Yao, A. K.-Y. Jen, Toward perovskite solar cell commercialization: A perspective and research roadmap based on interfacial engineering, Adv. Mater. 30 (2018) 1800455.

[10] N.-G. Park, M. Grätzel, T. Miyasaka, K. Zhu, K. Emery, Towards stable and commercially available perovskite solar cells, Nat. Energy 1 (2016) 16152.

[11] N. Ahn, D.-Y. Son, I.-H. Jang, S. M. Kang, M. Choi, N.-G. Park, Highly reproducible perovskite solar cells with average efficiency of 18.3% and best efficiency of 19.7% fabricated via lewis base adduct of lead (II) iodide, J. Am. Chem. Soc. 137 (2015) 8696-8699.

[12] F. Guo, S. Qiu, J. Hu, H. Wang, B. Cai, J. Li, X. Yuan, X. Liu, K. Forberich, C. J. Brabec, Y. H. Mai, A generalized crystallization protocol for scalable deposition of high-quality perovskite thin films for photovoltaic applications, Adv. Sci. 6 (2019) 1901067.

[13] J. Yang, C. Zuo, Y. Peng, Y. Yang, X. Yang, L. Ding, Large-area perovskite solar cells, Sci. Bull. 65 (2020) 872-875.

[14] S. Xiong, T. Hao, Y. Sun, J. Yang, R. Ma, J. Wang, S. Gong, X. Liu, L. Ding, M. Fahlman, Q. Bao, Defect passivation by nontoxic biomaterial yields 21% efficiency perovskite solar cells, J. Energy Chem. 55 (2021) 265-271.

[15] S. Wang, A. Wang, X. Deng, L. Xie, A. Xiao, C. Li, Y. Xiang, T. Li, L. Ding, F. Hao, Lewis acid/base approach for efficacious defect passivation in perovskite solar cells, J. Mater. Chem. A 8 (2020) 12201-12225.

[16] X. Deng, L. Xie, S. Wang, C. Li, A. Wang, Y. Yuan, Z. Cao, T. Li, L. Ding, F. Hao, Ionic liquids engineering for high-efficiency and stable perovskite solar cells, Chem. Eng. J. 398 (2020) 125594.

[17] A. J. Knight, A. D. Wright, J. B. Patel, D. P. McMeekin, H. J. Snaith, M. B. Johnston, L. M. Herz, Electronic traps and phase segregation in lead mixed-halide perovskite, ACS Energy Lett. 4 (2019) 75-84.

[18] G. Landi, H. C. Neitzert, C. Barone, C. Mauro, F. Lang, S. Albrecht, B. Rech, S. Pagano, Correlation between electronic defect states distribution and device performance of perovskite solar cells, Adv. Sci. 4 (2017) 1700183.

[19] D. W. deQuilettes, W. Zhang, V. M. Burlakov, D. J. Graham, T. Leijtens, A. Osherov, V. Bulović, H. J. Snaith, D. S. Ginger, S. D. Stranks, Photo-induced halide redistribution in organic-inorganic perovskite films, Nat. Commun. 7 (2016) 11683.

[20] F. Zhang, Q. Huang, J. Song, S. Hayase, J. Qu, Q. Shen, A new strategy for increasing the efficiency of inverted perovskite solar cells to more than 21%: High-humidity induced self-passivation of perovskite films, Sol. RRL 4 (2020) 2000149.

[21] F. Zhang, Q. Huang, J. Song, Y. Zhang, C. Ding, F. Liu, D. Liu, X. Li, H. Yasuda, K. Yoshida, J. Qu, S. Hayase, T. Toyoda, T. Minemoto, Q. Shen, Growth of amorphous passivation layer using phenethylammonium iodide for high-performance inverted perovskite solar cells, Sol. RRL 4 (2020) 1900243.

[22] H. Wang, F. Yang, Y. Xiang, S. Ye, X. Peng, J. Song, J. Qu, W.-Y. Wong, Achieving efficient inverted perovskite solar cells with excellent electron transport and stability by employing a ladder-conjugated perylene diimide dimer, J. Mater. Chem. A 7 (2019) 24191-24198.

[23] H. Wang, J. Song, Z. Li, L. Li, J. Li, X. Li, J. Qu, W.-Y. Wong, A linear conjugated tetramer as a surface modification layer to increase perovskite solar cell performance and stability, J. Mater. Chem. A 8 (2020) 11728-11733.

[24] H. Wang, F. Yang, N. Li, J. Song, J. Qu, S. Hayase, W.-Y. Wong, Interface engineering with a novel n-type small organic molecule for efficient inverted perovskite solar cells, Chem. Eng. J. 392 (2020) 123677.

[25] R. Wang, J. Xue, K.-L. Wang, Z.-K. Wang, Y. Luo, D. Fenning, G. Xu, S. Nuryyeva, T. Huang, Y. Zhao, J. L. Yang, J. Zhu, M. Wang, S. Tan, I. Yavuz, K. N. Houk, Y. Yang, Constructive molecular configurations for surface-defect passivation of perovskite photovoltaics, Science 366 (2019) 1509-1513.

[26] E. H. Jung, N. J. Jeon, E. Y. Park, C. S. Moon, T. J. Shin, T.-Y. Yang, J. H. Noh, J. Seo, Efficient, stable and scalable perovskite solar cells using poly(3-hexylthiophene), Nature 567 (2019) 511-515.

[27] C. Li, J. Yin, R. Chen, X. Lv, X. Feng, Y. Wu, J. Cao, Monoammonium porphyrin for blade-coating stable large-area perovskite solar cells with >18% efficiency, J. Am. Chem. Soc. 141 (2019) 6345-6351.

[28] H. Jiang, G. Jiang, W. Xing, W. Xiong, X. Zhang, B. Wang, H. Zhang, Y. Zheng, High current density and low hysteresis effect of planar perovskite solar cells via PCBM-doping and interfacial improvement, ACS Appl. Mater. Interfaces 10 (2018) 29954-29964.

[29] D. Bi, X. Li, J. V. Milić, D. J. Kubicki, N. Pellet, J. Luo, T. LaGrange, P. Mettraux, L. Emsley, S. M. Zakeeruddin, M. Grätzel, Multifunctional molecular modulators for perovskite solar cells with over 20% efficiency and high operational stability, Nat. Commun. 9 (2018) 4482.

[30] C.-C. Zhang, Z.-K. Wang, S. Yuan, R. Wang, M. Li, M. F. Jimoh, L.-S. Liao, Y. Yang, Polarized ferroelectric polymers for high-performance perovskite solar cells, Adv. Mater. 31 (2019) 1902222.

[31] J. Jiang, Q. Wang, Z. Jin, X. Zhang, J. Lei, H. Bin, Z.-G. Zhang, Y. Li, S. Liu, Polymer doping for high-efficiency perovskite solar cells with improved moisture stability, Adv. Energy Mater. 8 (2018) 1701757.

[32] D. Bi, C. Yi, J. Luo, J.-D. Décoppet, F. Zhang, S. M. Zakeeruddin, X. Li, A. Hagfeldt, M. Grätzel, Polymer-templated nucleation and crystal growth of perovskite films for solar cells with efficiency greater than 21%, Nat. Energy 1 (2016) 16142.

[33] J. Yang, C. Liu, C. Cai, X. Hu, Z. Huang, X. Duan, X. Meng, Z. Yuan, L. Tan, Y. Chen, High-performance perovskite solar cells with excellent humidity and thermo-stability via fluorinated perylenediimide, Adv. Energy Mater. 9 (2019) 1900198.

[34] T. Wu, Y. Wang, X. Li, Y. Wu, X. Meng, D. Cui, X. Yang, L. Han, Efficient defect passivation for perovskite solar cells by controlling the electron density distribution of donor-π-acceptor molecules, Adv. Energy Mater. 9 (2019) 1803766.

[35] V. M. Arivunithi, S. S. Reddy, V. G. Sree, H.-Y. Park, J. Park, Y.-C. Kang, E.-S. Shin, Y.-Y. Noh, M. Song, S.-H. Jin, Efficiency exceeding 20% in perovskite solar cells with side-chain liquid crystalline polymer-doped perovskite absorbers, Adv. Energy Mater. 8 (2018) 1801637.

[36] H. Wang, Y. Song, Y. Kang, S. Dong, J. Feng, Q. Dong, Reducing photovoltage loss at anode contact of methylammonium-free inverted perovskite solar cells by conjugated polyelectrolyte doping, J. Mater. Chem. A 8 (2020) 7309-7316.

[37] Y. Huan, C. Tan, B. Wu, X. Feng, W. Xu, D. Gao, A dopant-free zwitterionic conjugated polyelectrolyte as a hole-transporting and interfacial material for perovskite solar cells, Sol. RRL 4 (2020) 2000206.

[38] H. Choi, C.-K. Mai, H.-B. Kim, J. Jeong, S. Song, G. C. Bazan, J. Y. Kim, A. J. Heeger, Conjugated polyelectrolyte hole transport layer for inverted-type perovskite solar cells, Nat. Commun. 6 (2015) 7348.

[39] E. D. Jung, A. K. Harit, D. H. Kim, C. H. Jang, J. H. Park, S. Cho, M. H. Song, H. Y. Woo, Multiply charged conjugated polyelectrolytes as a multifunctional interlayer for efficient and scalable perovskite solar cells, Adv. Mater. 32 (2020) 2002333.

[40] B. Li, Y. Xiang, K. D. G. I. Jayawardena, D. Luo, Z. Wang, X. Yang, J. F. Watts, S. Hinder, M. T. Sajjad, T. Webb, H. Luo, I. Marko, H. Li, S. A. J. Thomson, R. Zhu, G. Shao, S. J. Sweeney, S. R. P. Silva, W. Zhang, Reduced bilateral recombination by functional

molecular interface engineering for efficient inverted perovskite solar cells, Nano Energy 68 (2020) 105249.

[41] W.-J. Huang, P.-H. Huang, S.-H. Yang, PCBM doped with fluorene-based polyelectrolytes as electron transporting layer for improving performance of planar heterojunction perovskite solar cells, Chem. Commun. 52 (2016) 13572-13575.

[42] Y. Cai, J. Cui, M. Chen, M. Zhang, Y. Han, F. Qian, H. Zhao, S. Yang, Z. Yang, H. Bian, T. Wang, K. Guo, M. Cai, S. Dai, Z. Liu, S. Liu, Multifunctional enhancement for highly stable and efficient perovskite solar cells, Adv. Funct. Mater. 30 (2020) 2005776.

[43] F. Li, X. Deng, F. Qi, Z. Li, D. Liu, D. Shen, M. Qin, S. Wu, F. Lin, S.-H. Jang, J. Zhang, X. Lu, D. Lei, C.-S. Lee, Z. Zhu, A. K.-Y. Jen, Regulating surface termination for efficient inverted perovskite solar cells with greater than 23% efficiency, J. Am. Chem. Soc. 142 (2020) 20134-20142.

[44] H. Si, C. Xu, Y. Ou, G. Zhang, W. Fan, Z. Xiong, A. Kausar, Q. Liao, Z. Zhang, A. Sarrar, Z. Kang, Y. Zhang, Dual-passivation of ionic defects for highly crystalline perovskite, Nano Energy 68 (2020) 104320.

[45] E. A. Alharbi, A. Y. Alyamani, D. J. Kubicki, A. R. Uhl, B. J. Walder, A. Q. Alanazi, J. Luo, A. Burgos-Caminal, A. Albadri, H. Albrithen, M. H. Alotaibi, J.-E. Moser, S. M. Zakeeruddin, F. Giordano, L. Emsley, M. Grätzel, Atomic-level passivation mechanism of ammonium salts enabling highly efficient perovskite solar cells, Nat. Commun. 10 (2019) 3008.

[46] J. J. Yoo, S. Wieghold, M. C. Sponseller, M. R. Chua, S. N. Bertram, N. T. P. Hartono, J. S. Tresback, E. C. Hansen, J.-P. Correa-Baena, V. Bulović, T. Buonassisi, S. S. Shin, M. G. Bawendi, An interface stabilized perovskite solar cell with high stabilized efficiency and low voltage loss, Energy Environ. Sci. 12 (2019) 2192-2199.

[47] X. Zheng, B. Chen, J. Dai, Y. Fang, Y. Bai, Y. Lin, H. Wei, X. C. Zeng, J. Huang, Defect passivation in hybrid perovskite solar cells using quaternary ammonium halide anions and cations, Nat. Energy 2 (2017) 17102.

[48] F. Yang, G. Kapil, P. Zhang, Z. Hu, M. A. Kamarudin, T. Ma, S. Hayase, Dependence of acetate-based antisolvents for high humidity fabrication of $CH_3NH_3PbI_3$ perovskite devices in ambient atmosphere, ACS Appl. Mater. Interfaces 10 (2018) 16482-16489.

[49] H. S. Kim, N. G. Park, Parameters affecting *I-V* hysteresis of $CH_3NH_3PbI_3$ perovskite solar cells: Effects of perovskite crystal size and mesoporous TiO_2 Layer, J. Phys. Chem. Lett. 5 (2014) 2927-2934.

[50] X. Gong, Q. Sun, S. Liu, P. Liao, Y. Shen, C. Grätzel, S. M. Zakeeruddin, M. Grätzel, M. Wang, Highly efficient perovskite solar cells with gradient bilayer electron transport materials, Nano Lett. 18 (2018) 3969-3977.

[51] F. Zhang, J. Song, R. Hu, Y. Xiang, J. He, Y. Hao, J. Liao, B. Zhang, P. Zeng, J. Qu, Interfacial passivation of the p-doped hole-transporting layer using general insulating polymers for high-performance inverted perovskite solar cells, Small 14 (2018) 1704007.

[52] H. Wang, F. Zhang, Z. Li, J. Zhang, J. Lian, J. Song, J. Qu, W.-Y. Wong, Naphthalene imide dimer as interface engineering material: An efficient strategy for achieving high-performance perovskite solar cells, Chem. Eng. J. 395 (2020) 125062.

[53] L. M. Herz, Charge-carrier mobilities in metal halide perovskites: Fundamental mechanisms and limits, ACS Energy Lett. 2 (2017) 1539-1548.